

Reconstructing the system coefficients for coupled harmonic oscillators

Jan Bartsch · Ahmed A. Barakat · Simon Buchwald ·
Gabriele Ciaramella · Stefan Volkwein · Eva M. Weig

Received: date / Accepted: date

Abstract Physical models often contain unknown functions and relations. In order to gain more insights into the nature of physical processes, these unknown functions have to be identified or reconstructed. Mathematically, we can formulate this research question within the framework of inverse problems. In this work, we consider optimization techniques to solve the inverse problem using Tikhonov regularization and data from laboratory experiments. We propose an iterative strategy that eliminates the need for laboratory experiments. Our method is applied to identify the coupling and damping coefficients in a system of oscillators, ensuring an efficient and experiment-free approach. We present our results and compare them with those obtained from an alternative, purely experimental approach. By employing our proposed strategy, we demonstrate a significant reduction in the number of laboratory experiments required.

Keywords inverse problems · system identification · interior-point method · coupled oscillators

Mathematics Subject Classification (2020) 34A30 · 34A55 · 34C15 · 93B30

Jan Bartsch
Department of Mathematics, University of Konstanz
Universitätsstraße 10, 78464 Konstanz, Germany
E-mail: jan.bartsch@uni-konstanz.de
ORCID: <https://orcid.org/0000-0002-8011-7422>

Ahmed A. Barakat
TUM School of Computation, Information and Technology, Technical University of Munich
Hans-Piloty-Str. 1(5901)/III, 85748 Garching b. München, Germany
Design and Production Engineering, Faculty of Engineering, Ain Shams University
El-Saray St. 1, Abbaseya, 11517 Cairo, Egypt.
E-mail: ahmed.barakat@tum.de
ORCID: <https://orcid.org/0000-0003-2197-1124>

Simon Buchwald
Department of Mathematics, University of Konstanz
Universitätsstraße 10, 78464 Konstanz, Germany
E-mail: simon.buchwald@uni-konstanz.de
ORCID: <https://orcid.org/0009-0004-2350-4399>

Gabriele Ciaramella
MOX Lab, Dipartimento di Matematica, Politecnico di Milano
Piazza Leonardo da Vinci 32, 20133, Milano, Italy
Member of GNCS Indam group
E-mail: gabriele.ciaramella@polimi.it
ORCID: <https://orcid.org/0000-0002-5877-4426>

Stefan Volkwein
Department of Mathematics, University of Konstanz
Universitätsstraße 10, 78464 Konstanz, Germany
E-mail: stefan.volkwein@uni-konstanz.de
ORCID: <https://orcid.org/0000-0002-1930-1773>

Eva Weig
TUM School of Computation, Information and Technology, Technical University of Munich
Hans-Piloty-Str. 1, 85748 Garching b. München, Germany
TUM Zentrum für QuantumEngineering (ZQE), Am Coulombwall 3a, 85748 Garching b. München, Germany
Munich Center for Quantum Science and Technology (MCQST), Schellingstr. 4, 80799 München, Germany E-mail: eva.weig@tum.de
ORCID: <https://orcid.org/0000-0003-4294-8601>

1 Introduction

The modeling of physical phenomena is crucial for understanding natural processes, allowing to predict behaviors and outcomes under various conditions. These models often rely on a set of coefficients that describe interactions and dynamics within the physical model. The accurate identification of these coefficients is essential for constructing reliable models that can simulate real-world behavior.

However, physical models often contain unknown functions and relations, posing significant challenges. These unknowns can stem from complex interactions within the model that are not directly observable. In order to gain more insights into the nature of physical processes, these unknown functions must be identified. This identification procedure involves adjusting the model parameters to ensure that the predictions of the model align with experimental observations. Consistency between these predictions and laboratory experiments is critical for validating both the accuracy of the reconstructed coefficients and the overall model.

Mathematically, we can formulate this research question within the framework of inverse problems; see, e.g., [17]. Inverse problems involve determining the causal factors from observed effects, and are often ill-posed, meaning that solutions may not exist, be unique, or depend continuously on the data. Regularization techniques, such as Tikhonov regularization, are employed to stabilize the solution of these problems by incorporating prior knowledge or additional constraints [17].

In this work, we apply this framework to a laboratory experiment and work with data generated in this experiment. We investigate a system of coupled linear driven and damped oscillators in which the damping and coupling coefficients are unknown. The linear oscillators correspond to the two fundamental vibrational modes of a nanomechanical resonator visualized in Figure 2.1(a). It consists of a long and thin nanostring which is a few hundred nanometers wide and thick and several tens of micrometers long and which vibrates at megahertz frequencies. The coupling between the modes is mediated by an electrical control field. Such nanoelectromechanical systems are employed, e.g., for sensing applications [2, 6, 13], such that a detailed understanding and modeling of its parameters is of crucial interest. Moreover, since the approach in this work is essentially mathematical, it can certainly be adjusted and extended to investigate the coupling interaction in other two-mode, or two-level, physical systems. In addition, similar signatures can be found, e.g., in cavity optomechanical systems or in circuit quantum electrodynamics [1, 10].

While the uncoupled system is very well understood [12, 23, 24], this is not the case for the coupled one. The identification of coefficients in the coupled oscillator and similar problems have been addressed in the literature [18, 25]. Our approach leverages both simulation and experimental data to enhance the accuracy of the coefficient reconstruction. It serves as a proof-of-principle demonstration and allows to be applied to more complex situations, where a conventional identification of coefficients via calibration measurements is no longer feasible.

Notice that the data from our experiments inherently include the effects of coupling. Therefore, we cannot measure the eigenfrequencies of the system and the coupling coefficient separately. On the contrary, through our experiments, we have only access to a hybridized quantity that contains both the eigenfrequencies and coupling coefficient. Therefore, these parameters and coefficients must be inferred through indirect methods that reconstruct them from measurement data while accounting for the coupling coefficient and eigenfrequency separately.

Our proposed strategy involves an iterative optimization technique using Tikhonov regularization to solve the inverse problem [14, 19]. To generate measurement data, we perform several experiments in the laboratory with different external excitation forces.

An important new contribution of our work is that the presented approach allows us to decrease the number of required laboratory experiments, reducing experimental costs and time. In particular, our approach needs fewer experiments than the one described in [3]. Furthermore, our experiments can be conducted easily and fast. Additionally, after fixing the physical model in which parameters should be identified, no additional physical concepts need to be taken into account. We compare our results to those obtained from a purely experimental approach that needs a larger number of experiments that are also more difficult to conduct [3]. By this comparison, we demonstrate the effectiveness of our method in reconstructing the system coefficients for coupled harmonic oscillators.

Moreover, our approach can be extended to different (also nonlinear) physical systems as long as they can be sufficiently well described by ordinary differential equations and the corresponding experiments can be conducted quickly. Also in view of this extension, our current work serves as a proof-of-principle.

The article is organized as follows. In Section 2, we introduce our specific framework and provide details on the transformation between the measurable model to which we have access in the experiments and the inaccessible one to which we want to identify the coefficients. We describe the physical background and laboratory setup in Section 3 before we explain in Section 4 how we scale the simulation data in order to compare them with the experimentally measured ones. In Section 5, we formulate the (regularized)

inverse problem and explain how we solve it. Afterward, we explain in [Section 6](#) how we solve the system of equations numerically. Finally, in [Section 7](#), we perform the final identification of the system coefficients by presenting our results and shortly compare it to a purely experimental approach in [Section 8](#). A section of conclusions completes this work.

Notation. For a vector $\mathbf{p} \in \mathbb{R}^n$, we denote by $\|\mathbf{p}\|_2$ the standard Euclidean norm: $\|\mathbf{p}\|_2 = \sqrt{\sum_{i=1}^n p_i^2}$. For a vector \mathbf{p} or a matrix A , we denote by \mathbf{p}^\top , or A^\top , their transpose. Whenever a vector or matrix is compared or divided by a vector or matrix, respectively, these operations have to be understood componentwise.

2 System of coupled oscillators

In this section, we introduce the setting of the considered parameter estimation problem that will be formulated in detail in [Section 5](#). We consider a vibrating nanostring that is modeled by a two-dimensional damped and driven harmonic oscillator. First, in [Section 2.1](#), the model is formulated in its standard form in which the coupling appears explicitly. However, the observation during measurement considers the system in transformed coordinates, where the pure mechanical eigenmodes of the oscillator are hybridized, or in a mathematical sense, where the stiffness matrix is diagonalized. Because of the hybridization of the physical coordinates, we need to transform the physical coordinates into hybridized modal coordinates, where the coupling remains only implicitly effective. We present the transformation of coordinates in detail in [Section 2.2](#). The structure of the driving forces that we use in the experiments is explained in [Section 2.3](#).

2.1 Standard model

We consider a coupled system of linear second-order ordinary differential equations (ODEs) in the physical coordinates q_1 and q_2 . The evolution of $\mathbf{q} := (q_1, q_2)^\top$ over a finite-time horizon $T_{\text{tot}} > 0$ is then given by the coupled linear second-order system

$$\begin{pmatrix} \ddot{q}_1(t) \\ \ddot{q}_2(t) \end{pmatrix} + \underbrace{\begin{pmatrix} 2\pi d_1 & 0 \\ 0 & 2\pi d_2 \end{pmatrix}}_{=: \mathcal{D}} \begin{pmatrix} \dot{q}_1(t) \\ \dot{q}_2(t) \end{pmatrix} + \underbrace{\begin{pmatrix} (2\pi f_1)^2 & -(2\pi\lambda)^2 \\ -(2\pi\lambda)^2 & (2\pi f_2)^2 \end{pmatrix}}_{=: \mathcal{C}} \begin{pmatrix} q_1(t) \\ q_2(t) \end{pmatrix} = \underbrace{\begin{pmatrix} b_1(t) \\ b_2(t) \end{pmatrix}}_{=: \mathbf{b}}, \quad t \in [0, T_{\text{tot}}], \quad (2.1)$$

with initial condition $q_1(0) = 0 = q_2(0)$ and $\dot{q}_1(0) = 0 = \dot{q}_2(0)$. Since the driving \mathbf{b} is assumed to be smooth, the solution \mathbf{q} to (2.1) is unique and smooth. For further analysis of such systems, see, e.g., [\[7, 27\]](#). As the observation of the system, we consider its Fourier transformation. To avoid transient effects within the Fourier transform, we will discard the transient phase $[0, T_{\text{trans}}]$, $0 \ll T_{\text{trans}} \ll T_{\text{tot}}$, and only consider the system in equilibrium for a fixed amount of time T , i.e., in the interval $[T_{\text{trans}}, T_{\text{trans}} + T]$, where we have defined $T := T_{\text{tot}} - T_{\text{trans}}$. Hence, the initial condition for (2.1) is just given for the sake of completeness and the fact that we need to specify it for the numerical simulations.

Notice that the constants d_1 and d_2 in the diagonal matrix \mathcal{D} are given in the unit [rad/s] and are related to frequencies f_1 and f_2 by $d_1 = f_1/Q_1$ and $d_2 = f_2/Q_2$, where Q_1 and Q_2 are the unitless so-called *quality factors*; cf. [\[27, \(3.38\)\]](#). We refer to d_1 and d_2 also as damping coefficients. These damping coefficients give the energy decay constant of the harmonic oscillator. Moreover, we denote with $\lambda > 0$ the coupling constant of the system.

2.2 Transformation of the system

The model in the form of (2.1) is used in theory to describe a system of coupled oscillators. However, it is not the observable system to which we have access in our laboratory experiments. In particular, we cannot measure the coupling coefficient λ or the frequencies f_1 and f_2 directly. We can only measure the hybridized modal coordinates \tilde{q}_1 and \tilde{q}_2 of the nanostring that result from a hybridization of q_1 and q_2 . They do not coincide with the physical coordinates \mathbf{q} for $\lambda > 0$. To derive the ODEs describing the behavior of the hybridized modal coordinates, we have to perform a coordinate transformation through a matrix \mathcal{J} from the original physical coordinates to the hybridized ones. The resulting system of ODEs has a diagonal stiffness matrix and therefore does not explicitly include the coupling coefficient.

To determine the transformation matrix \mathcal{J} , we follow a method similar to the one described in [\[11\]](#). Since \mathcal{C} in (2.1) is real and symmetric, its eigenvalues are real and we can diagonalize it using an orthogonal

matrix [26, Section 5.4]. The eigenvalues are given by

$$\eta_{\pm}^2 := \frac{1}{2} \left((2\pi f_1)^2 + (2\pi f_2)^2 \mp \sqrt{4(2\pi\lambda)^4 + ((2\pi f_1)^2 - (2\pi f_2)^2)^2} \right) \quad (2.2)$$

with corresponding orthogonal eigenvectors $v_+ = (v_+^1, v_+^2)$ and $v_- = (v_-^1, v_-^2)$. Since \mathcal{J} is orthogonal, it holds that $\mathcal{J}^{-1} = \mathcal{J}^\top$. We remark that the matrix \mathcal{J} can be assembled if one knows exactly the values of f_1, f_2 and λ . However, these values are unknown in the current case and we aim to estimate them by finding the correct transformation \mathcal{J} .

We introduce now the coordinate transformation between the hybridized modal coordinates $\tilde{\mathbf{q}} := (\tilde{q}_1, \tilde{q}_2)$ and the physical coordinates \mathbf{q} :

$$\tilde{\mathbf{q}}(t) = (\mathcal{J}\mathbf{q})(t). \quad (2.3)$$

The system describing the evolution of the hybridized modal coordinates, to which we have access in the experiments, has the following structure:

$$\ddot{\tilde{\mathbf{q}}}(t) + \tilde{\mathcal{D}}\dot{\tilde{\mathbf{q}}}(t) + \tilde{\mathcal{C}}\tilde{\mathbf{q}}(t) = \tilde{\mathbf{b}}(t), \quad t \in [0, T_{\text{tot}}] \quad (2.4a)$$

$$\mathbf{z} = \mathcal{F}(\tilde{\mathbf{q}}|_{[T_{\text{trans}}, T_{\text{tot}}]}). \quad (2.4b)$$

The observation \mathbf{z} is given as the Fourier transform \mathcal{F} of the time-dependent function $\tilde{\mathbf{q}}$ in the time interval $[T_{\text{trans}}, T_{\text{tot}}]$. In (2.4a), the matrices containing the damping and eigenfrequency, and the vector containing the external driving are given by

$$\tilde{\mathcal{D}} := \mathcal{J}\mathcal{D}\mathcal{J}^\top = \begin{pmatrix} \tilde{\mathcal{D}}_{11} & \tilde{\mathcal{D}}_{12} \\ \tilde{\mathcal{D}}_{21} & \tilde{\mathcal{D}}_{22} \end{pmatrix}, \quad \tilde{\mathcal{C}} := \mathcal{J}\mathcal{C}\mathcal{J}^\top = \begin{pmatrix} (2\pi\eta_+)^2 & 0 \\ 0 & (2\pi\eta_-)^2 \end{pmatrix}, \quad \tilde{\mathbf{b}}(t) = \begin{pmatrix} \tilde{b}(t) \\ \tilde{\tilde{b}}(t) \end{pmatrix},$$

where \tilde{b} will be specified in Section 2.3. Furthermore, the matrix $\tilde{\mathcal{D}}$ has the following structure

$$\tilde{\mathcal{D}} = \mathcal{J} \begin{pmatrix} 2\pi d_1 & 0 \\ 0 & 2\pi d_2 \end{pmatrix} \mathcal{J}^\top = \frac{2\pi}{v_+^1 + v_-^1} \begin{pmatrix} d_1 v_+^1 + d_2 v_-^1 & (-d_1 + d_2) v_-^1 v_+^1 \\ (-d_1 + d_2) & d_1 v_-^1 + d_2 v_+^1 \end{pmatrix}. \quad (2.5)$$

Notice that $\tilde{\mathcal{D}}$ is not diagonal. The off-diagonal elements can get small if the damping constants d_1 and d_2 get close to each other. Furthermore, we see that the diagonal elements in $\tilde{\mathcal{D}}$ are a (weighted) average of the damping constants d_1 and d_2 .

In our physical application, we can measure the eigenvalues η_{\pm} and the quality factors Q_{\pm} (cf. Section 4). Furthermore, we suppose that the diagonal elements of $\tilde{\mathcal{D}}$ are given by

$$\tilde{\mathcal{D}}_{11} = d_+ = \eta_+/Q_+, \quad \tilde{\mathcal{D}}_{22} = d_- = \eta_-/Q_-. \quad (2.6)$$

To regain the mathematical model (2.1) with explicitly including the coupling, we apply \mathcal{J}^\top from the left to (2.4a) and use (2.3) which results in

$$\ddot{\mathbf{q}}(t) + \mathcal{J}^\top \tilde{\mathcal{D}} \mathcal{J} \dot{\mathbf{q}}(t) + \mathcal{J}^\top \tilde{\mathcal{C}} \mathcal{J} \mathbf{q}(t) = \mathcal{J}^\top \tilde{\mathbf{b}}(t), \quad t \in [0, T_{\text{tot}}]. \quad (2.7)$$

For the right-hand side of (2.7) it holds that

$$\mathcal{J}^\top \tilde{\mathbf{b}}(t) = \mathbf{b}(t) = \begin{pmatrix} b_1(t) \\ b_2(t) \end{pmatrix} = \tilde{b}(t) \begin{pmatrix} v_-^1 + v_+^1 \\ v_-^2 + v_+^2 \end{pmatrix}.$$

Furthermore, recall that any orthogonal transformation matrix is an element of the orthogonal group $O(2)$ and hence of one of the following forms for $\theta \in (-\pi, \pi)$:

$$\begin{pmatrix} \cos(\theta) & -\sin(\theta) \\ \sin(\theta) & \cos(\theta) \end{pmatrix}, \quad \begin{pmatrix} -\cos(\theta) & \sin(\theta) \\ \sin(\theta) & \cos(\theta) \end{pmatrix}. \quad (2.8)$$

Thus, we aim to find the correct parameter $\theta \in (-\pi, \pi)$ to calculate the correct transformation \mathcal{J} . To indicate this fact, we write \mathcal{J}_θ for the transformation matrix given the parameter θ . In the numerical experiments, we use both forms and choose the one that leads to better results.

Notice that we do not have access to the elements in \mathcal{D} through the measurements. Hence, we include this in our parameter estimation problem. In summary, we search for the transformation matrix \mathcal{J}_θ and for the correct damping constants d_1, d_2 in (2.1). From the structure of $\tilde{\mathcal{D}}$, we know that $\tilde{\mathcal{D}}_{ii}$ contains information about d_i , $i = 1, 2$ (cf. (2.5)).

The unknowns in this setting are now the transformation parameter θ for \mathcal{J}_θ and the scalars d_1, d_2 constituting \mathcal{D} . To shorten the notation, we introduce the parameter vector containing the parameters we want to estimate as

$$\mathbf{p} := (\theta, d_1, d_2) \in \mathbb{R}^3. \quad (2.9)$$

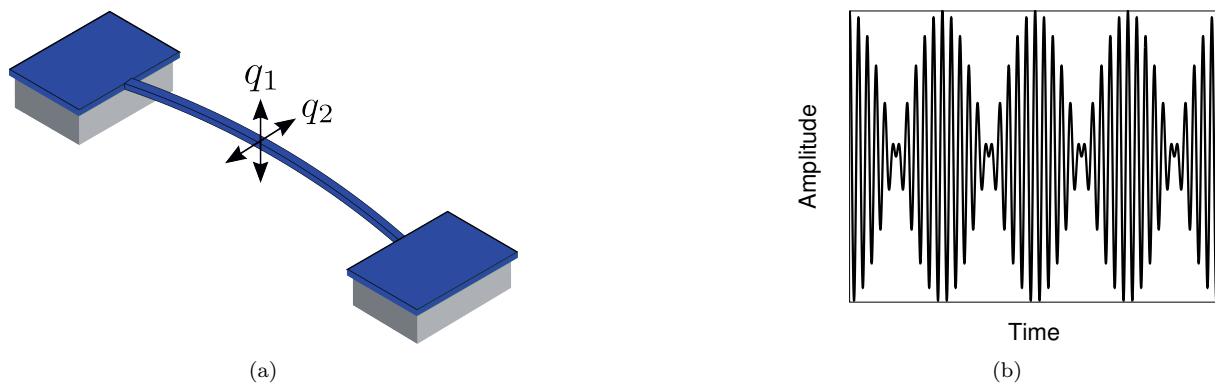


Fig. 2.1: (a) Vibration modes of the nanostring; (b) Form of external driving (cf. (2.13))

2.3 External driving forces

Motivated by [12, 15], we choose the following structure of the time-dependent driving forces (also called external excitation or controls).

$$\tilde{\mathbf{b}}(t) = \begin{pmatrix} \tilde{b}(t) \\ \tilde{b}(t) \end{pmatrix}, \quad \tilde{b}(t) = A \cos(2\pi u_1 t) + A \cos(2\pi u_2 t), \quad t \in [0, T_{\text{tot}}]. \quad (2.10)$$

We consider a control vector $\tilde{\mathbf{b}}$ with two identical components. This reflects the fact that both modes are exposed to the same excitation signal, assuming that both modes couple equally to the drive.

Here, $A > 0$ is the driving amplitude and $u_1, u_2 > 0$ are driving frequencies. We choose a fixed driving amplitude A and consider the driving frequencies u_1 and u_2 as input parameters.

In this setting, we know by trigonometric identities that for our controls it holds that

$$A \cos(2\pi u_1 t) + A \cos(2\pi u_2 t) = 2A \cos\left(\frac{2\pi(u_1 + u_2)t}{2}\right) \cos\left(\frac{2\pi(u_1 - u_2)t}{2}\right). \quad (2.11)$$

This phenomenon is also known as *beating* [27, Section 3.3.2]; see also Figure 2.1(b).

Notice that the frequency of one of the Cosine functions on the right-hand side is the difference between the two frequencies u_1 and u_2 . Since they are close to each other in our case, this results in a slow mode. Therefore, our time interval in the experiments and simulations should be long enough in order to catch both modes.

We choose to have $n_c \in \mathbb{N}$ of such driving forces with driving frequency pairs u_1^m, u_2^m for $m = 1, \dots, n_c$. To shorten the notation, we introduce the vectors $\mathbf{u} \in \mathbb{R}^2$ representing the input parameters:

$$\mathbf{u}^m = (u_1^m, u_2^m)^\top, \quad m = 1, \dots, n_c. \quad (2.12)$$

Furthermore, we define

$$\tilde{\mathbf{b}}^m(t) = (\tilde{b}^m(t), \tilde{b}^m(t))^\top, \quad \text{where} \quad \tilde{b}^m(t) = A \cos(2\pi u_1^m t) + A \cos(2\pi u_2^m t). \quad (2.13)$$

2.4 Drifting eigenfrequencies

An important observation that we made during our work is that the eigenfrequencies η_+ and η_- encounter drifts during the execution of the laboratory experiments, e.g., from slow temperature fluctuations. To include this in our model, we assume to know n_c eigenfrequencies that result from linear interpolation between the eigenfrequencies measured at the beginning and the end of our experiments. For this reason, we define $\tilde{\mathcal{C}}^m$ and \mathcal{C}^m as

$$\tilde{\mathcal{C}}^m := \begin{pmatrix} (2\pi\eta_+^m)^2 & 0 \\ 0 & (2\pi\eta_-^m)^2 \end{pmatrix}, \quad \mathcal{C}^m := \begin{pmatrix} (2\pi f_1^m)^2 & -(2\pi\lambda^m)^2 \\ -(2\pi\lambda^m)^2 & (2\pi f_2^m)^2 \end{pmatrix} \quad \text{for } m \in \{1, \dots, n_c\}. \quad (2.14)$$

We assume that \mathcal{D} and $\tilde{\mathcal{D}}$ do not depend on m . This is, an approximation, but we observe in our experiments that this assumption is suitable for the scope of this work.

3 Physical system and experimental setup

As described above, the reconstruction method presented in this work aims in particular to identify the coupling parameter λ between two orthogonal vibration modes of a nanomechanical string resonator. The resonator is made of a thin film of amorphous, stoichiometric silicon nitride (Si_3N_4) deposited on a fused silica wafer, and fabricated using top-down nanofabrication techniques. It has a length of $60\ \mu\text{m}$, a thickness of $100\ \text{nm}$ and a width of $250\ \text{nm}$, approximately. The experiment is performed at room temperature. In order to avoid damping of the nanostring’s vibrations from the surrounding medium, it is placed in a vacuum chamber at a pressure below 10^{-4} mbar (see [Figure 3.1\(b\)](#)).

The vibrational modes of the nanostring exhibit two orthogonal “polarizations” which are associated with a vibration along the out-of-plane and in-plane direction; cf. q_1 and q_2 in [Figure 2.1\(a\)](#). In principle, the nanostring, being a continuous system, exhibits an infinite number of vibrational modes in each of these polarization direction. In the context of this work, we will only be interested in its two fundamental modes. This is justified as the two fundamental modes exhibit similar eigenfrequencies which are spectrally well separated from all other higher-order harmonics. The lowest-lying out-of-plane and in-plane flexural mode q_1 and q_2 , schematically depicted in [Figure 2.1\(a\)](#), are hybridized into \tilde{q}_1 and \tilde{q}_2 by the coupling λ , where these vibration coordinates are rotated, but also orthogonal to each other [21]. The model describing the evolution in time of the two vibrational modes is given in (2.4).

Let us now describe the methods used for the vibrational excitation and measurement of the nanostring, which are illustrated in [Figure 3.1](#) and [Figure 3.2](#). The vibration is excited by means of an electric field surrounding the nanostring, induced by voltages applied between two electrodes positioned on either side as shown in [Figure 3.1\(a\)](#) and [Figure 3.2\(b\)](#). Since the nanostring is made of a dielectric material, the surrounding electric field will cause an electric polarization within, forming a collective electric dipole, which then follows the known dynamics of a dipole in an inhomogeneous electric field. The inhomogeneous electric field is engineered by placing the string out of the field’s axes of symmetry. In this way, a net dipole force is created in both vibrational coordinates, which then allows to induce the mechanical motion by combining a static (DC) with a dynamic (AC) voltage as depicted in [Figure 3.1](#); see [28]. In this experiment, the dynamic voltage V_{AC} consists of the sum of two excitation signals with two frequencies u_1 and u_2 close to each other (within the mode’s linewidth) according to (2.10). Notice that V_{DC} further determines the eigenfrequencies as well as other parameters of the system such as the linear coupling between the two modes and their damping rates, and is chosen according to the desired coupling strength.

The measurement of the string’s vibrations relies on the detection of the modulation in the capacitance between the two electrodes, which is caused by the vibration of the dielectric string in the inhomogeneous electric field. To resolve the resulting minute capacitance modulation, a microwave-cavity assisted heterodyne detection scheme is employed (see [20] for more detail). We employ a three-dimensional quarter-wave coaxial cavity that couples to the electric field between the electrodes via a loop antenna (see [Figure 3.1\(a\)](#) and [Figure 3.2\(a\)](#)). The cavity output signal (RF) is mixed with a reference signal (LO), amplified and filtered, before being recorded using a spectrum analyzer (see [Figure 3.1](#)).

A salient feature of our experimental setup is the tunability of the system with V_{DC} . In this work, we fixed the system’s parameters by selecting a specific bias voltage, $V_{\text{DC}} = -12\ \text{V}$. At this operating point, the two modes exhibit a sizable coupling strength [3]. In addition, their eigenfrequencies have been tuned to a situation where the transformation matrix \mathcal{J} is clearly distinct from the identity matrix, such that the coupling takes effect on the vibrational dynamics. It is in fact one advantage of our strategy that we can estimate the coupling parameter λ for a single V_{DC} voltage without the need to acquire information about the system at other V_{DC} voltages; see also [Sections 8](#) and [9](#).

4 Scaling of simulation and experiment

To ensure that the observations of the simulation and experimental setup are comparable, we need to scale the output of the simulations. The reason why we need this is that the physical quantities in the laboratory experiments are all measured in the unit [V] (volt). To determine the scaling factor, we measure the *frequency response function* (FRF) in the laboratory and compare it with the result of the computer simulations. Experimentally, the FRF for a specific mode is obtained by exciting the nanostring with several frequencies close to the eigenfrequency of the mode. At each excitation frequency, the amplitude response of the nanostring is recorded. This procedure is also known as *sweeping*. Then we use a software to determine the resonance frequency η_{\pm} , the amplitude A_{\pm} of the peak, and the quality factor Q_{\pm} . To compute the scaling, the shape of the squared FRF is important. This should have a *Lorentzian* shape with a maximum peak A_{\pm} at the resonant frequency η_{\pm} ; this shape is also called *Cauchy distribution* in

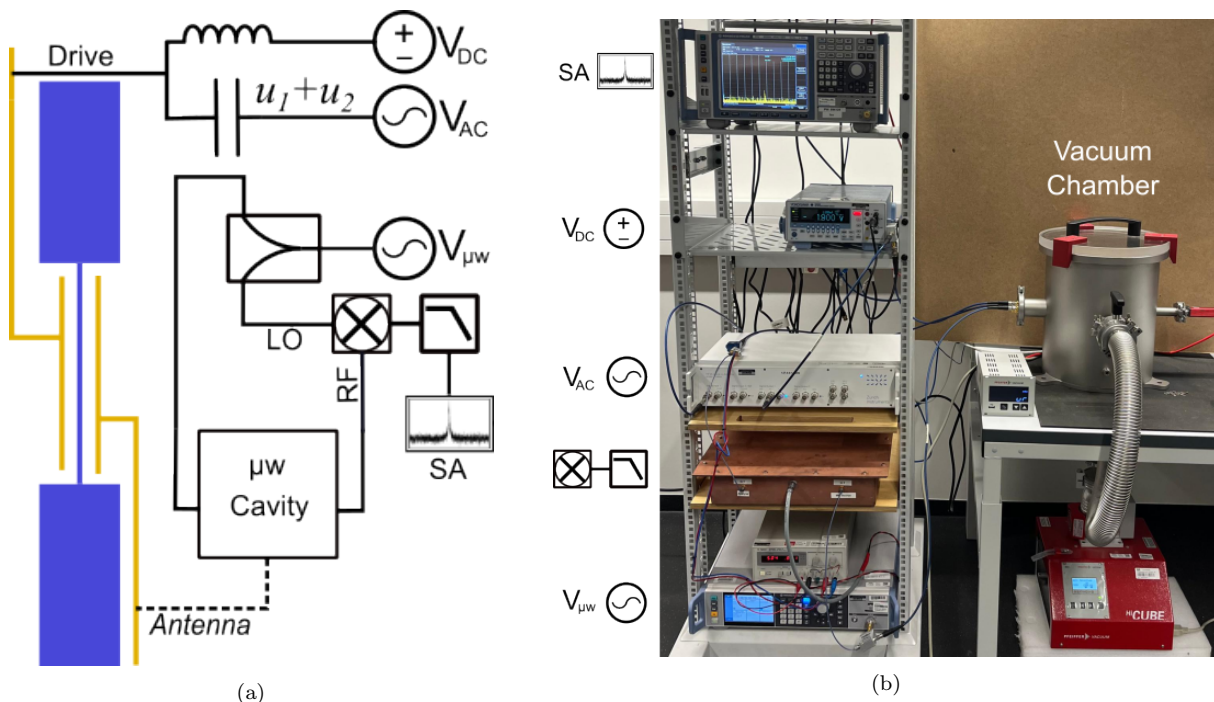


Fig. 3.1: Experimental measurement setup. (a) Schematic of the measurement setup used to drive and detect the vibration of the nanostring. (b) Photograph of the measurement setup, depicting major electronic components from Figure 3.1(a) as well as the vacuum chamber hosting the microwave cavity and the nanostring chip.

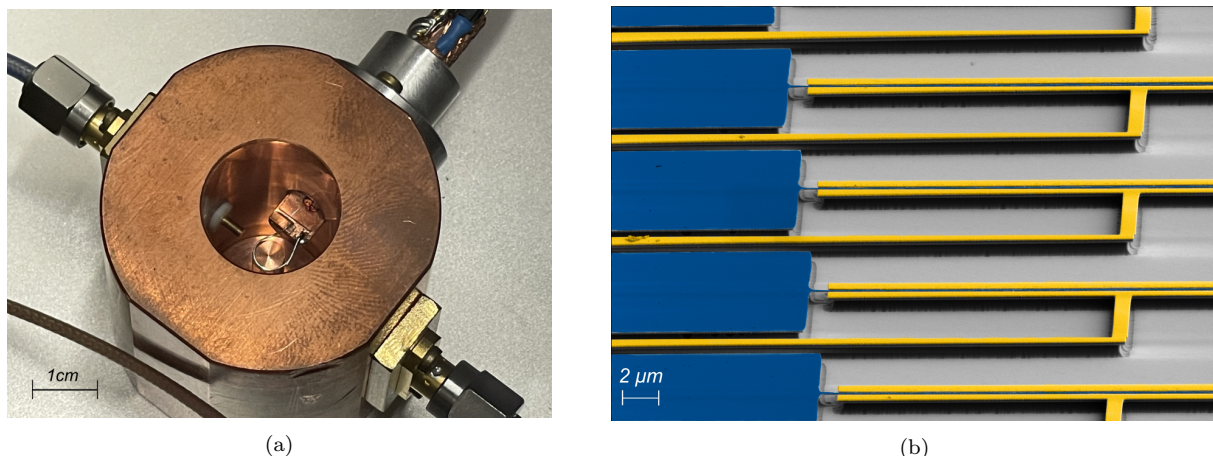


Fig. 3.2: Microwave cavity and nanostring chip. (a) Photograph of the coaxial quarter-wave microwave cavity. The loop antenna coupling the cavity mode to the electrical field surrounding the nanostring as well as the (transparent) nanostring chip can be discerned above and next to the center stub, respectively. (b) Scanning electron micrograph of a representative device depicting a partial view of several nanostrings (blue) between pairs of electrodes (yellow).

the realm of probability density functions; see, e.g., [16]. The scaling factor is now the ratio between the peak amplitudes of the displacements in equilibrium in the laboratory experiment and the simulations.

This Lorentzian shape is defined by the following formula

$$\rho_L(f; \eta_{\pm}, d_{\pm}, A_{\pm}) := \frac{A_{\pm} - \xi}{1 + \left(\frac{2\pi f - 2\pi\eta_{\pm}}{d_{\pm}}\right)^2} \quad \text{for } f > 0, \quad (4.1)$$

where d_{\pm} is a scale parameter that specifies the full-width at half-maximum (FWHM) and equals the damping parameter. As introduced in (2.6), we have the relation $Q_{\pm} = \eta_{\pm}/d_{\pm}$. Furthermore, $0 < \xi \ll 1$ is the noise level of the lab data.

Remark 4.1 An important observation is that the scaling also depends on the unknown damping coefficients d_1, d_2 and transformation matrix \mathcal{T}_θ ; see also [Algorithm 5.1](#) below. \diamond

We summarize our procedure to get our \mathbf{p} -dependent scaling factor $\chi_{\mathbf{p}}$ in [Algorithm 4.1](#).

Algorithm 4.1 (FRF Calibration Laboratory/Simulation)

Require: parameter vector $\mathbf{p} \in \mathbb{R}^3$, FRF data set from laboratory experiment $\mathbf{C}_L \in \mathbb{R}^{N_{\text{FRF,L}}}$, frequency discretization $\{f_S^1, \dots, f_S^{N_{\text{FRF,S}}}\}$ for simulation of sweeping

- 1: Initialize empty list $\mathbf{C}_S \leftarrow \{\}$;
- 2: **for** $j = 1, \dots, N_{\text{FRF,S}}$ **do**
- 3: Simulate the system (2.4a) using \mathbf{p} and $\cos(2\pi f_S^j t)$ as input;
- 4: Append the maximum amplitude $\max_{t \in [T_{\text{trans}}, T_{\text{tot}}]} |\tilde{q}_1(t)|$ of \tilde{q}_1 to \mathbf{C}_S ;
- 5: **end for**
- 6: Set $\chi_{\mathbf{p}} \leftarrow \max_{1 \leq i \leq N_{\text{FRF,L}}} (\mathbf{C}_L)_i / \max_{1 \leq i \leq N_{\text{FRF,S}}} (\mathbf{C}_S)_i$;
- 7: **return** $\chi_{\mathbf{p}}$

5 Parameter identification problem

Recall that we aim at estimating the damping coefficients d_1, d_2 in \mathcal{D} and transformation matrix \mathcal{T}_θ . The latter one will lead to estimates of the matrices $\mathcal{C}^m = \mathcal{T}_\theta^\top \tilde{\mathcal{C}}^m \mathcal{T}_\theta$ for $m = 1, \dots, n_c$, where $\tilde{\mathcal{C}}^m$ is known (cf. [Section 2](#)). To stress the dependence of \mathcal{D} and \mathcal{T}_θ on the unknown parameter vector

$$\mathbf{p} = (\theta, d_1, d_2)$$

defined in (2.9), we use the notation $\mathcal{T}_{\mathbf{p}} := \mathcal{T}_\theta$ and

$$\mathcal{D}_{\mathbf{p}} := \begin{pmatrix} 2\pi d_1 & 0 \\ 0 & 2\pi d_2 \end{pmatrix}, \quad \tilde{\mathcal{D}}_{\mathbf{p}} := \mathcal{T}_{\mathbf{p}} \mathcal{D}_{\mathbf{p}} \mathcal{T}_{\mathbf{p}}^\top.$$

We have the following structure of the ODEs in the final identification:

$$\ddot{\mathbf{q}}^m(t) + \mathcal{D}_{\mathbf{p}} \dot{\mathbf{q}}^m(t) + \mathcal{T}_{\mathbf{p}}^\top \tilde{\mathcal{C}}^m \mathcal{T}_{\mathbf{p}} \mathbf{q}^m(t) = \mathcal{T}_{\mathbf{p}}^\top \tilde{\mathbf{b}}^m(t), \quad t \in [0, T_{\text{tot}}], \quad m \in \{1, \dots, n_c\} \quad (5.1)$$

with known $\tilde{\mathcal{C}}^m, \tilde{\mathbf{b}}^m$ and unknown $\mathcal{T}_{\mathbf{p}}, \mathcal{D}_{\mathbf{p}}$.

Notice that in (5.1) the untransformed matrix $\mathcal{D}_{\mathbf{p}}$ and the transformed matrix $\tilde{\mathcal{C}}^m$ appear. The reason for this is given by the limitations and possibilities of the measurements. More specifically, we can measure all entries of the diagonal matrix $\tilde{\mathcal{C}}^m$ but only the diagonal elements of $\tilde{\mathcal{D}}_{\mathbf{p}}$. However, $\tilde{\mathcal{D}}_{\mathbf{p}}$ is not diagonal (cf. (2.5)). Hence, we reconstruct the untransformed matrix $\mathcal{D}_{\mathbf{p}}$.

Next, we denote by $\mathbf{z}_{\mathbf{p}}^{u^m} := \mathcal{F}(\mathcal{T}_{\mathbf{p}} \mathbf{q}^m|_{[T_{\text{trans}}, T_{\text{tot}}]})$, $m = 1, \dots, n_c$, the Fourier transformations within the time interval $[T_{\text{trans}}, T_{\text{tot}}]$ of the solutions of (5.1) with transformation $\mathcal{T}_{\mathbf{p}}$ of the structure (2.8) generated with θ , using d_1, d_2 as damping coefficients, and applying the control parameters $\{\mathbf{u}^m\}_{m=1}^{n_c}$ (cf. (2.12)). Moreover, we define $\{\mathbf{z}_{\star}^{u^m}\}_{m=1}^{n_c}$ as the experimental data generated in the laboratory using the same control parameters $\{\mathbf{u}^m\}_{m=1}^{n_c}$.

Our goal is to minimize the difference between the two peaks of the Fourier transformation. The reason that there appear exactly two peaks is that we are in the linear setting. Here, our solution is the superposition of harmonic oscillators under a periodic force for which the behavior is well-known and given as the sum of periodic functions; see, e.g., [27, Chapter 4]. Within our linear setting, we cannot change the locations of the peaks in equilibrium since they are fixed by the control/driving frequency [27, Chapter 4]. Hence, with our parameter vector \mathbf{p} , we can only influence the amplitude.

Furthermore, we need to scale the simulation in order to be able to compare the amplitudes of the simulations with the ones of the laboratory experiments; see [Section 4](#) above. The procedure to get the scaling factor $\chi_{\mathbf{p}}$ is described in [Algorithm 4.1](#). Notice that $\chi_{\mathbf{p}}$ depends on \mathbf{p} . Therefore, we need to execute [Algorithm 4.1](#) each time the coefficient vector \mathbf{p} is changed.

We consider the following definition of the deviation between simulation and experiment.

Definition 5.1 Let $z_{\mathbf{p}}^u$ be the amplitude in the Fourier transform of the simulations using the parameter vector \mathbf{p} and the driving frequency $u > 0$. Furthermore, let z_{\star}^u be the corresponding amplitude in the experiments. Then, we define the *relative deviation* as

$$\mathbf{e}(z_{\mathbf{p}}^u, z_{\star}^u) := \frac{|z_{\mathbf{p}}^u - z_{\star}^u|}{z_{\star}^u}, \quad (5.2)$$

where $|\cdot|$ denotes the absolute value. Furthermore, we define the vector containing all relative deviations

$$\mathfrak{E}_{n_c}(\mathbf{z}_p^u, \mathbf{z}_\star^u) := \left(\mathfrak{e}(z_{p_1}^{u^m}, z_{\star_1}^{u^m}) \right)_{m=1}^{n_c} \in \mathbb{R}^{2n_c}. \quad (5.3)$$

This definition of the deviation is used in the objective \mathcal{J} below. We introduce the set of admissible parameters \mathcal{P}_{ad} as

$$\mathcal{P}_{\text{ad}} := \{ \mathbf{p} \in \mathbb{R}^3 \mid \mathbf{p}_{\min} \leq \mathbf{p} \leq \mathbf{p}_{\max} \}, \quad (5.4)$$

with fixed parameter vectors $\mathbf{p}_{\min} \leq \mathbf{p}_{\max}$ (componentwise). Notice that \mathcal{P}_{ad} is non-empty, convex, and compact in \mathbb{R}^3 . Incorporating the admissible set \mathcal{P}_{ad} is mainly due to being able to apply standard methods from optimization theory.

Our objective is given by the sum of the two following functions

$$\mathcal{J}_{\text{fit}}(\mathbf{p}, \mathbf{z}_p, \chi_p) := \sum_{m=1}^{n_c} \mathfrak{e}(\chi_p z_p^{u^m}, z_\star^{u^m}) + \mathfrak{e}(\chi_p z_p^{u_2^m}, z_\star^{u_2^m}), \quad \mathcal{J}_{\text{reg}}^\nu(\mathbf{p}) := \frac{\nu}{2} \|\mathbf{p} - \mathbf{p}^{\text{ref}}\|_2^2. \quad (5.5)$$

Now the identification (or parameter estimation) problem is given by

$$\min \mathcal{J}(\mathbf{p}) := \mathcal{J}_{\text{fit}}(\mathbf{p}, \mathbf{z}_p, \chi_p) + \mathcal{J}_{\text{reg}}^\nu(\mathbf{p}) \quad \text{subject to} \quad \mathbf{p} \in \mathcal{P}_{\text{ad}}, \quad (5.6)$$

where $\mathbf{z}_p = \mathcal{F}(\mathcal{J}_p \mathbf{q}_p|_{[T_{\text{trans}}, T_{\text{tot}}]})$, \mathbf{q}_p fulfills (5.1) and χ_p is the scaling factor (cf. Section 4) for $\mathbf{p} = (\theta, d_1, d_2)$. Problem (5.6) is a nonconvex inverse problem with a Tikhonov regularization parameter $\nu \geq 0$ [14]. Furthermore, we choose some references for the parameters in the vicinity of where we expect the optimal solution to be located. In particular, we take $\mathbf{p}_1^{\text{ref}} = \theta^{\text{ref}} = \pi/2 + \pi/8$ since we expect from experimental results that the correct coupling has the corresponding order of magnitude. Furthermore, we choose $\mathbf{p}_2^{\text{ref}} = d_1^{\text{ref}} = \tilde{\mathcal{D}}_{11}/2\pi$, and $\mathbf{p}_3^{\text{ref}} = d_2^{\text{ref}} = \tilde{\mathcal{D}}_{22}/2\pi$, since we do not expect too much change in the damping constants compared to measurements $\tilde{\mathcal{D}}_{11}$ and $\tilde{\mathcal{D}}_{22}$. We remark, that there exists a solution to (5.6) by standard arguments; see, e.g., [5, 9, 17, 19].

To solve (5.6), we apply an iterative strategy commonly used to tackle inverse problems. First, we choose an initial guess $\mathbf{p}^0 \in \mathcal{P}_{\text{ad}}$ for the parameter vector and an initial Tikhonov regularization parameter ν_0 . Then, we solve (5.6) with these quantities, shrink the regularization parameter, and check a termination criterion. If it is not fulfilled, we start again solving (5.6) with the updated parameter vector as the initial guess and with the updated regularization parameter. We summarize the procedure in Algorithm 5.1.

Algorithm 5.1 (Iterative reconstruction procedure)

Require: Laboratory data $\{z_\star^{u^m}\}_{m=1}^{n_c}$, $\ell_{\max} \in \mathbb{N}$, tolerance $\text{tol} > 0$, regularization parameter update $\beta \in (0, 1)$;

- 1: Initial guess $\mathbf{p}^0 \in \mathcal{P}_{\text{ad}}$, $\ell \leftarrow 0$, initialize $E \gg \text{tol}$, initialize regularization parameter $\nu_0 \gg 0$;
- 2: **while** $E > \text{tol}$ **and** $\ell < \ell_{\max}$ **do**
- 3: Solve (5.6) with `fmincon` using initial guess \mathbf{p}^ℓ and $\nu = \nu_\ell$ to get $\mathbf{p}^{\ell+1}$; \triangleright needs run of Algorithm 4.1
- 4: Set $\nu_{\ell+1} = \beta \nu_\ell$; \triangleright update regularization parameter
- 5: Set $E \leftarrow \|\mathbf{p}^{\ell+1} - \mathbf{p}^\ell\|_2 + |\mathcal{J}_{\text{fit}} - \mathcal{J}_{\text{reg}}^{\nu_{\ell+1}}|$;
- 6: Set $\ell \leftarrow \ell + 1$;
- 7: **end while**
- 8: **return** \mathbf{p}^ℓ

A schematic visualization of our whole strategy to estimate the coupling and damping coefficients in a system of oscillators is given in Figure 5.1. Starting from our model (5.1), we apply the same drive signals in the experiment and in simulations. Finally, the results are used in Algorithm 5.1 in order to solve the parameter estimation problem (5.6).

6 Numerical implementation

In this section, we describe our strategy to numerically solve (5.1) over the long time horizon T_{tot} . This is needed for two reasons: First, we have to integrate over the transient phase T_{trans} since we need to reach a steady state; second, we need a sufficiently long signal to detect the correct frequencies numerically in the Fourier transformation; third, we have to deal with the beating phenomenon described in Section 2.3 and hence need a sufficiently large T to correctly resolve all frequencies in the signal.

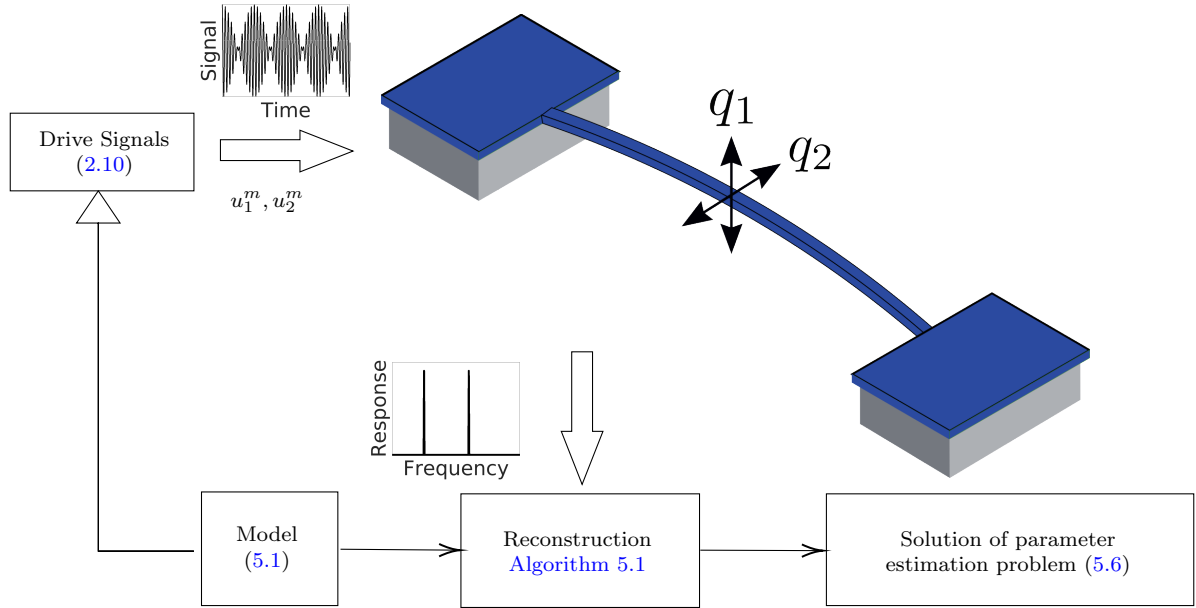


Fig. 5.1: Schematic visualization of the proposed strategy.

Δt	10^{-6}	\parallel	T	$3 \cdot 10^4$	\parallel	T_{trans}	$2 \cdot 10^3$
β	0.1	\parallel	ν_0	10^{-1}	\parallel		

Table 6.1: Simulation parameters and hyperparameters.

Since we consider a system of linear ODEs, we can apply the *Laplace transformation* \mathcal{L} in order to get its analytical solution. For fixed $m \in \{1, \dots, n_c\}$, the Laplace transformation $\hat{q}_i^m(s) = \mathcal{L}\{q_i^m\}(s)$ ($i = 1, 2$) is given as the solution of

$$\begin{pmatrix} s^2 + (\mathcal{D}_{\mathbf{p}})_{11} s + (\mathcal{C}_{\mathbf{p}}^m)_{11} & (\mathcal{D}_{\mathbf{p}})_{12} s + (\mathcal{C}_{\mathbf{p}}^m)_{12} \\ (\mathcal{D}_{\mathbf{p}})_{21} s + (\mathcal{C}_{\mathbf{p}}^m)_{21} & s^2 + (\mathcal{D}_{\mathbf{p}})_{22} s + (\mathcal{C}_{\mathbf{p}}^m)_{22} \end{pmatrix} \begin{pmatrix} \hat{q}_1(s) \\ \hat{q}_2(s) \end{pmatrix} = \begin{pmatrix} ((\mathcal{J}_{\mathbf{p}})_{11} + (\mathcal{J}_{\mathbf{p}})_{21}) \hat{b}^m(s) \\ ((\mathcal{J}_{\mathbf{p}})_{12} + (\mathcal{J}_{\mathbf{p}})_{22}) \hat{b}^m(s) \end{pmatrix}, \quad (6.1)$$

with coordinate transformation matrix $\mathcal{J}_{\mathbf{p}}$, $\mathcal{C}_{\mathbf{p}}^m := \mathcal{J}_{\mathbf{p}}^\top \tilde{\mathcal{C}}^m \mathcal{J}_{\mathbf{p}}$ and

$$\hat{b}^m(s) := \mathcal{L}\{\tilde{b}^m\}(s) = A \left(\frac{2\pi u_1^m}{(2\pi u_1^m)^2 + s^2} + \frac{2\pi u_2^m}{(2\pi u_2^m)^2 + s^2} \right).$$

After solving (6.1), we utilize the built-in Matlab function `ilaplace` to compute \mathbf{q} and the function `rectangularPulse` in the time interval $[T_{\text{trans}}, T_{\text{trans}} + T]$ to have a signal of finite length and discarding the transient phase.

The last step is to apply the built-in Matlab function `fourier` in order to get the Fourier transformation of the function. We then evaluate the Fourier transformation at the frequencies at which we also have experimental data. For the generation of the frequency interval in which we want to evaluate the Fourier transformation, we split the time interval $[T_{\text{trans}}, T_{\text{trans}} + T]$ into N_t equidistant cells of length $\Delta t = T/N_t$. The frequency interval is then given by $[f_a, f_b] = \frac{1}{\Delta t T} [0, T/2]$, where T is the length of the time interval. In Table 6.1, we present the parameters that we use for the simulation. Moreover, we use $\mathbf{p}_{\min} = [-2\pi, -0.1, -0.1]$ and $\mathbf{p}_{\max} = [2\pi, 0.1, 0.1]$.

7 Identification using the proposed framework

In this section, we present the results of our proposed framework obtained with laboratory data to validate its effectiveness. For our main example, we use $n_c = 5$ control pairs with driving frequencies $\{u_i^m\}_{i=1, m=1}^{2, n_c}$ in (2.10) as they are given in Table 7.1. These frequencies are fixed manually within the linewidth (that is $2d_1$) of the resonance mode in order to gain a sufficiently large signal-to-noise ratio. Moreover, they should not be too close together to be able to distinguish the response signals by the spectrum analyzer. Applying the driving frequencies to the real-world experiment, we obtain the laboratory data $\{\mathbf{z}_*^m\}_{m=1}^{n_c}$.

u_1^1		6.94016		u_2^1		6.94036
u_1^2		6.94018		u_2^2		6.94034
u_1^3		6.94020		u_2^3		6.94032
u_1^4		6.94024		u_2^4		6.94028
u_1^5		6.94025		u_2^5		6.94027

Table 7.1: Driving frequencies for the \tilde{q}_1 mode in MHz.

To use this data in our numerical optimization, we first subtract the noise $\xi > 0$ (defined as the average of the data). The actual average noise level ξ of the experiment is between $0.2 \mu\text{V}$ and $0.3 \mu\text{V}$.

We solve the constrained minimization problem (5.6) for a fixed ν using the Matlab built-in function `fmincon` which uses the interior-point method; see, e.g., [22]. Choosing an initial guess $\mathbf{p}^0 \equiv 0$ we rely for \mathbf{p}^{ref} on our experience as described in Section 5. In Table 7.2 we report the transformation parameter θ and the differences \bar{d}_1 , \bar{d}_2 calculated from the reference parameter vector \mathbf{p}^{ref} ; i.e. $\bar{d}_1 = d_1 - \mathbf{p}_1^{\text{ref}}$, $\bar{d}_2 = d_2 - \mathbf{p}_2^{\text{ref}}$. As tolerance `tol`, we use machine precision, the algorithm considered nine iterations, and the final regularization ν_9 was 10^6 .

With the optimal parameter θ , we compute the matrices \mathcal{C}^m (cf. (2.14)), calculate the averaged quantities $\langle \lambda \rangle := 1/n_c \sum_{m=1}^{n_c} \lambda^m$, and analogously $\langle f_1 \rangle$, $\langle f_2 \rangle$, and present the average together with the uncertainty interval in Table 7.2.

The most interesting one for this work is the coupling parameter λ . See also the discussion in Section 8.

f_1		6.9522 ± 0.0001 MHz		f_2		7.0156 ± 0.0001 MHz		λ		0.6474 ± 0.0002 MHz
θ		1.9498 [-]		\bar{d}_1		1.5828 μHz		\bar{d}_2		6.4871 μHz

Table 7.2: Optimal estimated coefficients.

The comparison of the laboratory measurements and the simulation results using the initial parameters \mathbf{p}^0 and the optimal ones \mathbf{p}^{opt} resulting from Algorithm 5.1 are presented in Figure 7.1. The vertical lines show the driving frequencies. In Figure 7.1(a), we plot the experimental data (solid, orange) and the simulated data (dashed, blue) for the unreconstructed parameters \mathbf{p}^0 . As expected, we observe the two peaks that correspond to the excitation frequencies in all plots. The peaks have in theory a delta shape since they are Fourier transformations of an essentially sinusoidal signal. However, since we work with a finite resolution in simulation and experiment, this approximation results in a small non-zero width of the peak.

With our optimization procedure, a better agreement of the amplitude of the peaks for simulation and experiment is obtained. In Figure 7.1(b), we plot the experimental data and the simulated data with the reconstructed \mathbf{p}^{opt} provided by Algorithm 5.1. In fact, in Figure 7.1(b) we see that the agreement of the simulated and the experimental data is significantly enhanced when using the optimal parameters \mathbf{p}^{opt} . This can be observed in particular by the length of the errorbars. They demonstrate the difference between the maxima of the peaks in the experimental and simulation data.

To quantify the improvement, we plot in Figure 7.2(a) the deviation introduced in Definition 5.1 for the initial guess (black) and the reconstructed parameter (red) over the driving frequencies. The gray area visualizes the range of the drift of the eigenfrequencies during the execution of the laboratory experiment (cf. Section 2.4). The initial eigenfrequency is denoted by η_+^1 and the final one η_+^5 . The deviations corresponding to the specific control pair are tagged with a distinct marker shape (from $m = 1, \dots, 5$: bullet, triangle, pentagon, diamond, square). These shapes stay the same throughout the paper. We observe that we can decrease the relative deviation for each control pair. More in detail, the average relative deviation decreases from 0.7 to 0.17 (dashed lines). In Figure 7.2(b), we plot the relative improvement of the deviation between experimental and simulated data, this is $\mathfrak{E}_{\mathbf{p}^{\text{opt}}}/\mathfrak{E}_{\mathbf{p}^0}$ (cf. Definition 5.1), over the driving frequencies. We see that the deviation between the experimental data and the simulations using \mathbf{p}^{opt} is, on average, only 20% of the deviation between the experimental data and the simulation using \mathbf{p}^0 .

In Figure 7.3, we visualize the convergence behavior of Algorithm 5.1. As expected, we see in Figure 7.3(a) that at the first iterations, the value of θ is close to θ^{ref} and then converges to a value different from θ^{ref} . In all three panels, we observe that after the third iteration, the algorithm seems to have converged and only small improvements are made afterwards.

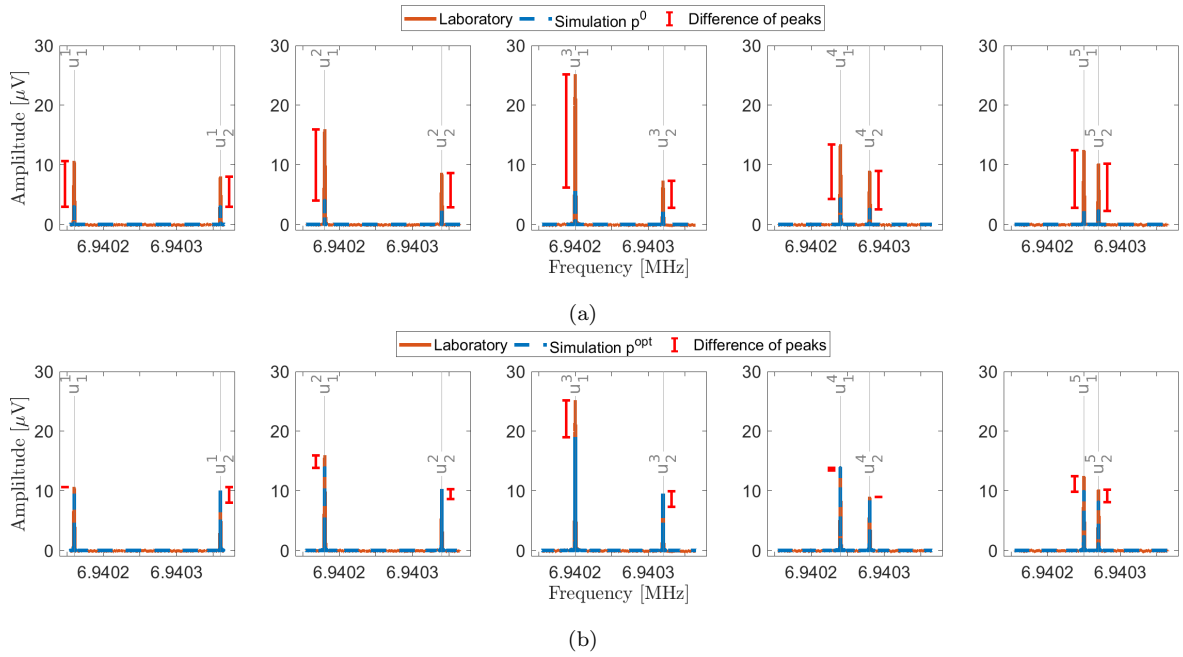


Fig. 7.1: Experimental data (solid, orange) and simulated data (dashed, blue) applying the driving frequencies given in Table 7.1. The red errorbars indicate the difference between the amplitudes of the peaks of experimental and simulation data. The vertical lines depict the control frequencies; (a) before the reconstruction (using $\mathbf{p}^0 \equiv 0$); (b) after the reconstruction using \mathbf{p}^{opt} ; for the reconstructed parameters see Table 7.2 and for simulation parameters see Table 6.1.

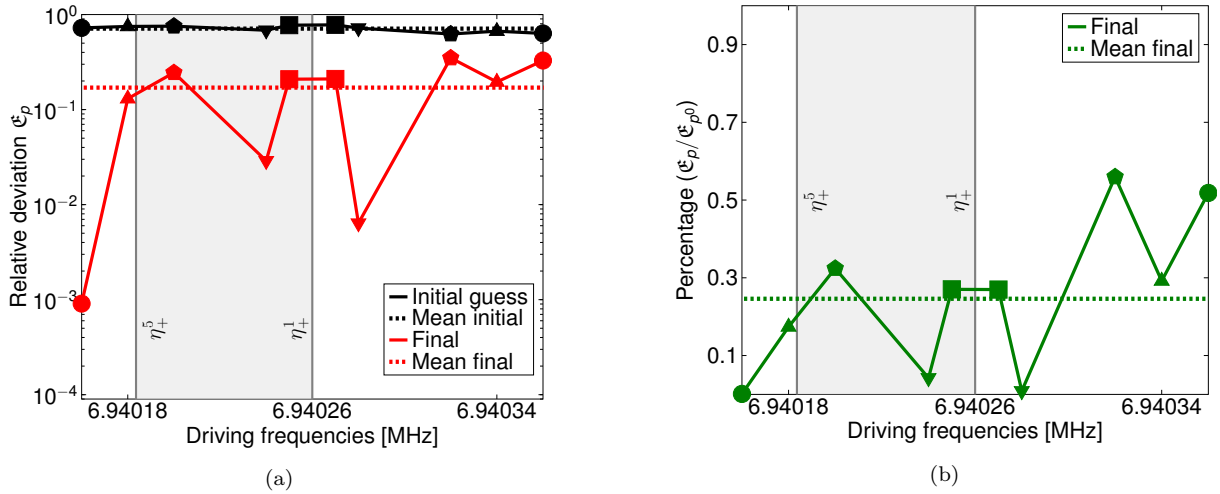


Fig. 7.2: Deviation plots of the result of Algorithm 5.1. The different marker shapes depict the different control pairs (cf. Table 7.1); (a) Relative deviation for driving frequencies (cf. Definition 5.1) before ($\mathfrak{E}_{\mathbf{p}^0}$, black) and after ($\mathfrak{E}_{\mathbf{p}^{\text{opt}}}$, red) the reconstruction process; (b) Deviation improvement $\mathfrak{E}_{\mathbf{p}^{\text{opt}}}/\mathfrak{E}_{\mathbf{p}^0}$ in percent (cf. Definition 5.1).

In Figure 7.4(a), we plot the λ^m , $m = 1, \dots, n_c$ and the average $\langle \lambda \rangle$. We observe that the difference between the λ^m and $\langle \lambda \rangle$ is quite small and in the order of magnitude of the drifting eigenfrequencies. In Figure 7.4(b), we plot the deviation introduced in Definition 5.1 over the control frequency pairs. We observe that the deviation is higher than the average for the third control pair and the least for the fourth control pair.

To validate the optimal parameters found by Algorithm 5.1, we perform a second test. For this, we choose control frequencies located around the eigenfrequency η_- of the mode \tilde{q}_2 . Then, we solve (5.6) once with fixed (small) regularization parameter ν and use the controls given in Table 7.3.

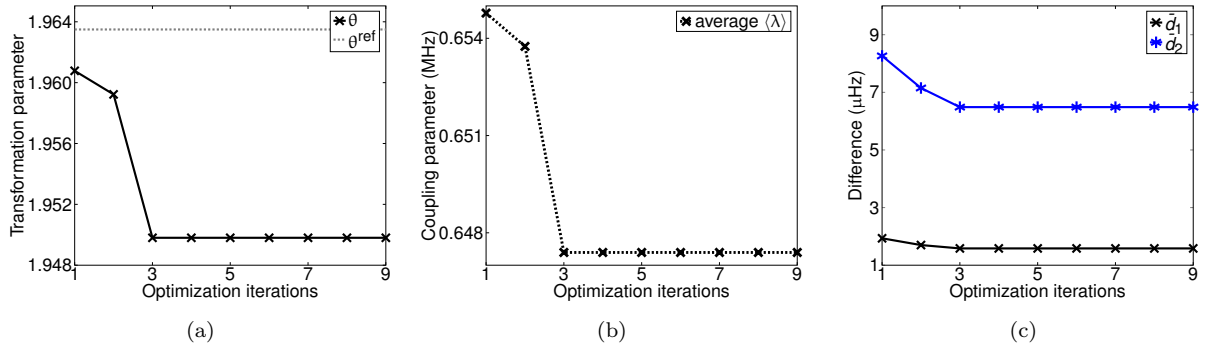


Fig. 7.3: Convergence history of [Algorithm 5.1](#). (a) Convergence of θ ; (b) Convergence of averaged $\langle \lambda \rangle$; (c) Convergence of corrections \bar{d}_1 , \bar{d}_2 to the damping parameters.

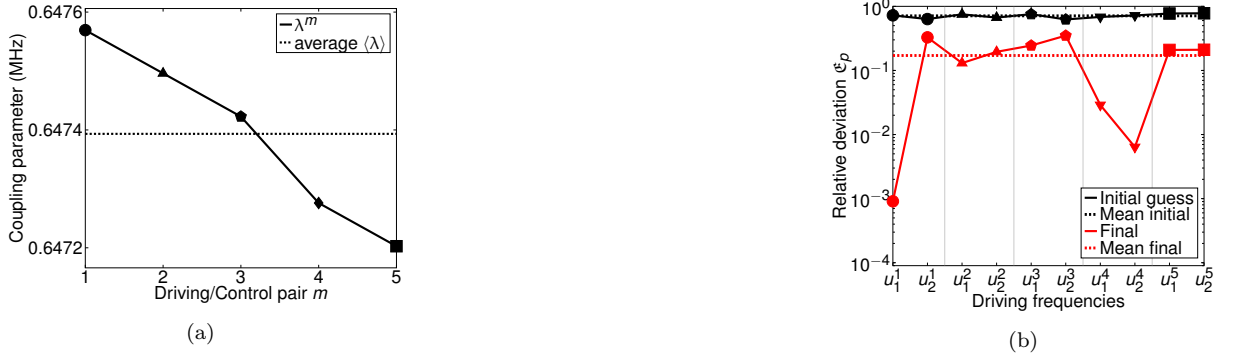


Fig. 7.4: Results of final identification for \tilde{q}_1 mode. The different marker shapes depict the different control pairs given in [Table 7.1](#); (a) Coupling constant λ^m for controls pairs and average $\langle \lambda \rangle$; (b) Deviation for the initial guess ($\mathcal{E}_{\mathbf{p}^0}$, black) and in the final iteration ($\mathcal{E}_{\mathbf{p}^{\text{opt}}}$, red) ordered by control pairs (cf. [Figure 7.2\(a\)](#)).

u_1^1		7.02750		u_2^1		7.02770
u_1^2		7.02752		u_2^2		7.02768
u_1^3		7.02754		u_2^3		7.02766
u_1^4		7.02758		u_2^4		7.02762
u_1^5		7.02759		u_2^5		7.02761

Table 7.3: Driving frequencies around the eigenfrequency η_- in MHz.

In [Figures 7.5](#) and [7.6](#), we show the results of this optimization. In [Figure 7.5](#), we plot similar to [Figure 7.1](#) the experimental data (solid, orange) and the simulated data (dashed, blue) for the unreconstructed parameters \mathbf{p}^0 . The vertical lines show the driving frequencies. In [Figure 7.5\(a\)](#) present the Fourier transform for the \tilde{q}_2 mode given the initial guess \mathbf{p}^0 and in [Figure 7.5\(b\)](#) for the optimized parameters \mathbf{p}^{opt} . In all plots, the lengths of the error indicate the difference in the amplitude of the peaks in the experimental and simulation data.

In [Figure 7.6\(a\)](#), we plot the relative deviation defined in [Definition 5.1](#) for the initial guess (black) and the optimized parameters (red). Furthermore, the gray area depicts the region of the drift of the eigenfrequencies. Notice that in this experiment, the drift is larger than for the \tilde{q}_1 mode. In [Figure 7.6\(b\)](#), we plot the improvement of the deviation similar to [Figure 7.2\(b\)](#). Also here we see that we can improve the parameters of the model but not as well as for the \tilde{q}_1 mode. More specifically, the relative deviation decreases from 0.74 to 0.27 (dashed lines). Further, we observe that the reconstructed parameters also slightly differ from the ones of the \tilde{q}_1 mode. Notice that the driving frequencies are farther away from the (shifted) eigenfrequency η_-^5 as in the previous experiment. Hence, we cannot expect a similar or better behavior.

In [Table 7.4](#), we present the resulting estimated parameters analogous to [Table 7.2](#).

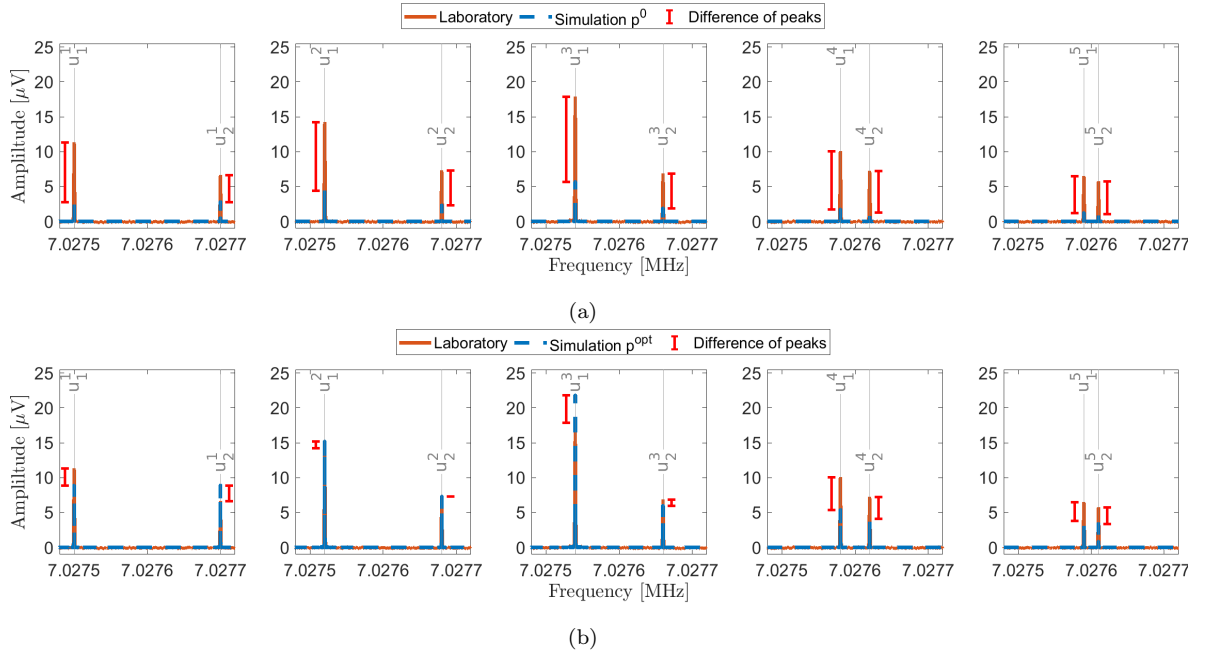


Fig. 7.5: Experimental data (solid, orange) and simulated data (dashed, blue) applying the driving frequencies given in Table 7.3. The red errorbars indicate the difference between the amplitudes of the peaks of experimental and simulation data. The vertical lines depict the control frequencies; (a) before the reconstruction (using $\mathbf{p}^0 \equiv 0$); (b) after the reconstruction using \mathbf{p}^{opt} ; for the reconstructed coefficients see Table 7.4 and for simulation parameters Table 6.1.

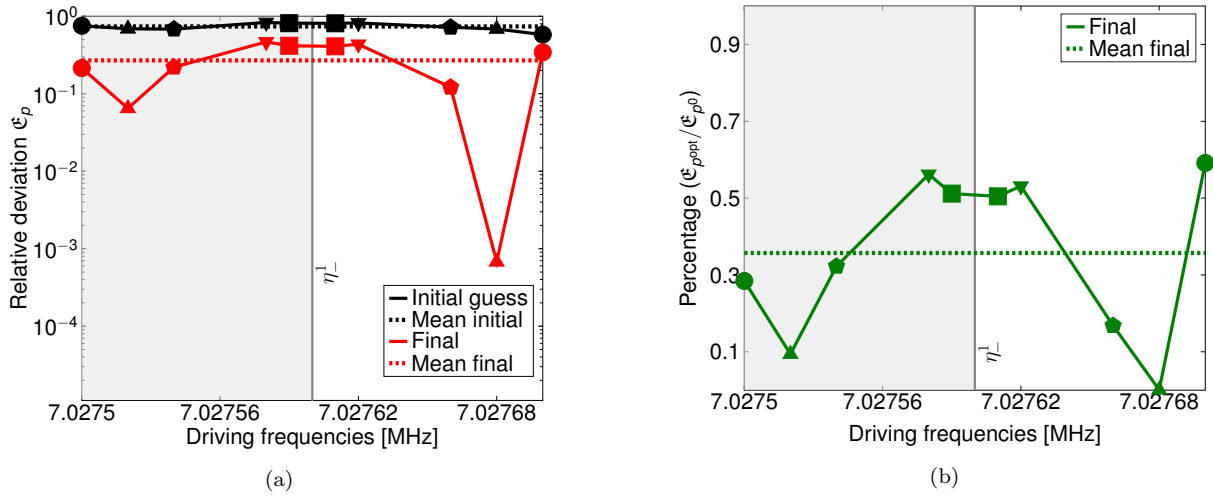


Fig. 7.6: Deviation plots and coupling for \tilde{q}_2 mode. The different marker shapes depict the different control pairs (cf. Table 7.3); (a) Relative deviation \mathcal{E}_p (cf. Definition 5.1); (b) Deviation improvement in percent $\mathcal{E}_{p^{\text{opt}}}/\mathcal{E}_{p^0}$;

f_1	6.9582 ± 0.0001 MHz	f_2	7.009 ± 0.0001 MHz	λ	0.7016 ± 0.0002 MHz
θ	2.0406 [-]	\bar{d}_1	6.247 mHz	\bar{d}_2	2.906 mHz

Table 7.4: Reconstructed coefficients for \tilde{q}_2 mode.

8 Comparison with another independent experiment

In this section, we compare our results of Section 7 with those of another experimental approach in [3]. In this cited work, the authors use the same string (see Supp. Mat. of [3]) as well as the same experimental setup, thus ensuring the measurement of the same system dynamics. While in the current work, we use a lock-in amplifier to generate the two excitation signals, the authors in [3] used a noise drive that allows

to excite all frequencies within a certain band at the same time. Furthermore, another harmonic signal is added for a parametric excitation in that experiment, which was required for that experimental approach. All other setup details are exactly the same including, in the first place, the investigated sample and the coupled actuation and read-out systems. Furthermore, the work in [3] ranges over an interval of DC voltages V_{DC} from -32 to 32 V, where the coupling coefficient λ is deduced by a thorough measurement and analysis of PNMS based on a mathematical model.

This parallel between both contributions elevates the certainty in both results since the two approaches are intrinsically different. While the cited approach relies on the physical modeling of the system as well as on the use of a coupling-dependent physical phenomenon, called the parametric normal mode splitting (PNMS), to estimate the coupling coefficient [3], we rely here on a purely mathematical approach, that is, no physical modeling is added in the presented work except for the consideration of a linearly coupled two-mode oscillating system.

Regarding the results, the deduced coupling coefficient from the experiment in [3] yielded 0.8604 MHz while that of the work presented here gives 0.6474 MHz and 0.7016 MHz for \tilde{q}_1 and \tilde{q}_2 , respectively, nevertheless representing the same coupling coefficient. The values deduced from the current work and that of [3] are found to be of the same order of magnitude with a difference of about 20%, which is near to the tolerance given for the numerical experiments inside the current work (see Figure 7.4(a)). Arriving at these relatively near results despite using two totally different methodologies, and remarkably despite the usual drifts in experimental results across non-simultaneously performed experiments, supports our findings in this work and thus provides an important asset in extending our methodology to the investigation of other system parameters.

In addition, the work in [3] required a thorough mathematical modeling for the underlying physics, and an additional experiment ranging over a range of bias voltages to determine the implicit parameters of the system. However, in the presented work, we solely require a fast executable experiment at a given bias voltage, without any need for modeling the physical nature of the coupling itself.

In summary, we can state that our approach greatly reduces the experimental overhead in terms of complexity of the experiment, measurement time, number of measurements required, and therefore also the cost of the experiments.

9 Conclusion/Discussion

This work presents an efficient approach for reconstructing system coefficients in coupled harmonic oscillators through an iterative optimization method based on Tikhonov regularization and considering actual data from laboratory experiments. The success of our method lies in its ability to automatically combine simulation and experimental data, leveraging the structure of the inverse problem. By utilizing this approach, our method achieved estimates of the coupling and damping coefficients that coincide very well with a completely different physical approach.

Our reconstructed parameters are within the correct order of magnitude, indicating that our method reliably captures the system's underlying behavior. Given the inherent noise and complexity of real-world experiments, we cannot expect to achieve absolute precision. However, the results show a high level of consistency and alignment with theoretical expectations, which is sufficient for many practical applications.

Another significant achievement of this method is the reduction of laboratory time. By employing a combined approach of simulations and minimal experiments, we drastically cut down the number of physical tests required. This not only saves time but also reduces the cost associated with running numerous experiments in a laboratory setting.

Importantly, one of the strengths of our method is that it does not require deep knowledge of the underlying physics of the system. Instead, the method focuses on reconstructing the system coefficients from observed data, making it broadly applicable to other similar systems. This versatility, combined with its efficiency, makes it a valuable tool for system identification and optimization tasks in various scientific and engineering contexts.

One possible improvement of our method is to find optimized driving frequencies selected in a greedy manner. This approach has been discussed and applied to small problems in [8]. By choosing these frequencies carefully, it is possible to capture the necessary dynamics with even less experimentation. However, given the current setup, the constraints on the driving frequencies are so stringent that further optimization is unlikely to yield significantly different results.

Furthermore, this approach can also be applied to models in which an unknown nonlinearity has to be reconstructed. In this case, one can for example choose a set of basis functions that can be used to approximate the nonlinearity. The optimization problem is then to find the coefficients in a linear combination of the basis elements that lead to the best agreement of simulation and experimental data;

see, e.g., [4] for further information on this procedure applied to a semilinear elliptic partial differential equation.

Statements and Declarations

Funding. This work was funded by the Deutsche Forschungsgemeinschaft within SFB 1432, Project-ID 425217212.

Author contributions. All authors worked together in formulating the identification problem, and in writing and editing the manuscript. J.B. worked on the algorithm to solve the identification problem, implemented the simulation codes, and conducted the final identification. A.B. contributed to the physical modeling and conducted the laboratory experiments. S.B. provided contributions to the strategies used in the optimization procedure. G.C. and S.V. supervised the project and provided conceptualization from a mathematical point of view. E.W. supervised the project and provided conceptualization from a physical point of view. G.C., S.V., and E.W. procured funding within the SFB1432.

Competing interests. The authors have no relevant financial or non-financial interests to disclose.

References

1. ASPELMEYER, M., KIPPENBERG, T. J., AND MARQUARDT, F. Cavity optomechanics. *Reviews of Modern Physics* 86, 4 (Dec. 2014), 1391–1452. Publisher: American Physical Society.
2. BACHTOLD, A., MOSER, J., AND DYKMAN, M. I. Mesoscopic physics of nanomechanical systems. *Reviews of Modern Physics* 94, 4 (2022), 045005.
3. BAKARAT, A. A., CHOWDHURY, A., LE, A. T., AND WEIG, E. M. Parametric normal mode splitting for coupling strength estimation. *in preparation* (2024).
4. BARTSCH, J., BUCHWALD, S., CIARAMELLA, G., AND VOLKWEIN, S. Reconstruction of unknown nonlinear operators in semilinear elliptic models using optimal inputs. *arXiv:2405.12153, submitted to Math. Control. Relat. F.* (2024).
5. BARTSCH, J., DENK, R., AND VOLKWEIN, S. Adjoint-based calibration of nonlinear stochastic differential equations. *Appl. Math. Opt.* 90, 50 (2024).
6. BARZANJEH, S., XUEREB, A., GRÖBLACHER, S., PATERNOSTRO, M., REGAL, C. A., AND WEIG, E. M. Optomechanics for quantum technologies. *Nature Physics* 18, 1 (Jan. 2022), 15–24.
7. BORZI, A. *Modelling with Ordinary Differential Equations – A Comprehensive Approach*. Chapman & Hall/CRC Numerical Analysis and Scientific Computing. CRC Press, Boca Raton, FL, 2020.
8. BUCHWALD, S., CIARAMELLA, G., AND SALOMON, J. Analysis of a greedy reconstruction algorithm. *SIAM J. Control Optim.* 59, 6 (2021), 4511–4537.
9. BURGER, M., AND MÜHLHUBER, W. Iterative regularization of parameter identification problems by sequential quadratic programming methods. *Inverse Probl.* 18, 4 (2002), 943–969.
10. CLERK, A. A., LEHNERT, K. W., BERTET, P., PETTA, J. R., AND NAKAMURA, Y. Hybrid quantum systems with circuit quantum electrodynamics. *Nature Physics* 16, 3 (Mar. 2020), 257–267.
11. FRIMMER, M., AND NOVOTNY, L. The classical Bloch equations. *Am. J. Phys.* 82, 10 (Oct. 2014), 947–954.
12. GAJO, K., RASTELLI, G., AND WEIG, E. M. Tuning the nonlinear dispersive coupling of nanomechanical string resonators. *Phys. Rev. B* 101, 7 (Feb. 2020), 075420.
13. GUO, M.-L., FANG, J.-W., CHEN, J.-F., LI, B.-L., CHEN, H., ZHOU, Q., WANG, Y., SONG, H.-Z., ARUTYUNOV, K. Y., GUO, G.-C., ET AL. Mode coupling in electromechanical systems: Recent advances and applications. *Advanced Electronic Materials* 9, 7 (2023), 2201305.
14. HABER, E., ASCHER, U. M., AND OLDENBURG, D. On optimization techniques for solving nonlinear inverse problems. *Inverse Probl.* 16, 5 (2000), 1263–1280.
15. HUBER, J. S., RASTELLI, G., SEITNER, M. J., KÖLBL, J., BELZIG, W., DYKMAN, M. I., AND WEIG, E. M. Spectral evidence of squeezing of a weakly damped driven nanomechanical mode. *Phys. Rev. X* 10, 2 (Apr. 2020), 021066.
16. JOHNSON, N. L., KOTZ, S., AND BALAKRISHNAN, N. *Continuous multivariate distributions*, second ed., vol. 1. Wiley New York, 1994.
17. KIRSCH, A. *An introduction to the mathematical theory of inverse problems*, third ed., vol. 120 of *Applied Mathematical Sciences*. Springer, Cham, 2021.
18. KRALEMANN, B., CIMPONERIU, L., ROSENBLUM, M., PIKOVSKY, A., AND MROWKA, R. Phase dynamics of coupled oscillators reconstructed from data. *Phys. Rev. E* 77, 6 (June 2008), 066205.
19. KUNISCH, K., AND ZOU, J. Iterative choices of regularization parameters in linear inverse problems. *Inverse Probl.* 14, 5 (1998), 1247–1264.
20. LE, A. T. *3D Microwave Cavity-Controlled Nanoelectromechanical Systems: for Cavity Electromechanics and Quantum Sensing*. PhD thesis, Technische Universität München, 2023.
21. MEIROVITCH, L. *Fundamentals of vibrations*. McGraw-Hill, Boston, 2001.
22. NOCEDAL, J., AND WRIGHT, S. J. *Numerical optimization*, second ed. Springer Series in Operations Research and Financial Engineering. Springer, New York, 2006.
23. OCHS, J. S., BONESS, D. K. J., RASTELLI, G., SEITNER, M., BELZIG, W., DYKMAN, M. I., AND WEIG, E. M. Frequency comb from a single driven nonlinear nanomechanical mode. *Phys. Rev. X* 12, 4 (Oct. 2022), 041019.
24. OCHS, J. S., RASTELLI, G., SEITNER, M., DYKMAN, M. I., AND WEIG, E. M. Resonant nonlinear response of a nanomechanical system with broken symmetry. *Phys. Rev. B* 104, 15 (Oct. 2021), 155434.
25. PANAGGIO, M. J., CIOCANEL, M.-V., LAZARUS, L., TOPAZ, C. M., AND XU, B. Model reconstruction from temporal data for coupled oscillator networks. *Chaos* 29, 10 (Oct. 2019), 103116.
26. SHORES, T. S. *Applied Linear Algebra and Matrix Analysis*. Undergraduate Texts in Mathematics. Springer, New York, 2007.
27. SINGIRESU, S. R., ET AL. *Mechanical Vibrations*. Addison Wesley Boston, MA, 1995.
28. UNTERREITHMEIER, Q. P., WEIG, E. M., AND KOTTHAUS, J. P. Universal transduction scheme for nanomechanical systems based on dielectric forces. *Nature* 458, 7241 (2009), 1001–1004.